Improving the lens design and performance of a contemporary electromagnetic shock wave lithotripter

Andreas Neisius[a,b,1], Nathan B. Smith[c,1], Georgy Sankin[c], Nicholas John Kuntz[a], John Francis Madden[d], Daniel E. Fovargue[e], Sorin Mitran[e], Michael Eric Lipkin[a], Walter Neal Simmons[c], Glenn M. Preminger[a], and Pei Zhong[a,c,2]

[a]Division of Urologic Surgery and [d]Department of Pathology, Duke University Medical Center, Durham, NC 27710; [b]Department of Urology, Universitätsmedizin Mainz, Johannes Gutenberg University, 55131 Mainz, Germany; [c]Department of Mechanical Engineering and Materials Science, Duke University, Durham, NC 27708; and [e]Department of Mathematics, University of North Carolina at Chapel Hill, Chapel Hill, NC 27599

Edited by Alexis T. Bell, University of California, Berkeley, CA, and approved February 20, 2014 (received for review October 31, 2013)

The efficiency of shock wave lithotripsy (SWL), a noninvasive first-line therapy for millions of nephrolithiasis patients, has not improved substantially in the past two decades, especially in regard to stone clearance. Here, we report a new acoustic lens design for a contemporary electromagnetic (EM) shock wave lithotripter, based on recently acquired knowledge of the key lithotripter field characteristics that correlate with efficient and safe SWL. The new lens design addresses concomitantly three fundamental drawbacks in EM lithotripters, namely, narrow focal width, nonidealized pulse profile, and significant misalignment in acoustic focus and cavitation activities with the target stone at high output settings. Key design features and performance of the new lens were evaluated using model calculations and experimental measurements against the original lens under comparable acoustic pulse energy (E_+) of 40 mJ. The −6-dB focal width of the new lens was enhanced from 7.4 to 11 mm at this energy level, and peak pressure (41 MPa) and maximum cavitation activity were both realigned to be within 5 mm of the lithotripter focus. Stone comminution produced by the new lens was either statistically improved or similar to that of the original lens under various in vitro test conditions and was significantly improved in vivo in a swine model (89% vs. 54%, $P = 0.01$), and tissue injury was minimal using a clinical treatment protocol. The general principle and associated techniques described in this work can be applied to design improvement of all EM lithotripters.

electromagnetic lithotripter | lens modification | stone fragmentation

Since its inception in the early 1980s, shock wave lithotripsy (SWL) has become the treatment of choice for more than 80% of nephrolithiasis patients because of its noninvasiveness compared with open surgery or other minimally invasive surgical procedures (1). During this period, the prevalence of kidney stones in the United States has risen significantly from 3.8% in 1980 to 8.8% in 2010 (2, 3), in parallel with the increase in metabolic syndrome (e.g., obesity and diabetes) of the population (4, 5). Previous technological improvements in SWL were mainly focused on operator convenience and patient comfort, as exemplified by the use of dry coupling and large source aperture in contemporary lithotripters (6), except for the introduction of electromagnetic (EM) technology for shock wave generation in the late 1980s (7). Currently, EM lithotripters have eclipsed electrohydraulic (EH) lithotripters, such as the first-generation Dornier HM3, as the preferred technology in SWL (8). The main advantages of EM (over EH) lithotripters are their reproducibility in acoustic output, large dynamic range in peak positive pressure (p_+) and acoustic pulse energy, and elimination of consumable parts (i.e., electrodes) during or between treatments. Despite this, there is growing clinical evidence to suggest that contemporary EM lithotripters are less efficient in fragmenting stones than the original HM3 (8, 9). This unexpected setback has been attributed to two general features of the EM lithotripters, namely, narrow −6-dB focal width (FW), which is defined as full width at half maximum peak pressure, and nonidealized pulse profile (10). Specifically, most modern EM lithotripters have small FW (4–7 mm) with high p_+ (up to 100 MPa) compared with large FW (10–12 mm) with low p_+ (~40 MPa) of the HM3 (11). In addition, as a result of current oscillation in the EM coil, a typical acoustic pulse produced by EM lithotripters has a second compressive wave following its primary shock front and tensile tail. This second compressive wave in the lithotripter shock wave (LSW) profile (absent from the HM3) suppresses cavitation activity in the urine surrounding the target stone, which is known to play a critical role in producing fine fragments (12). Recent studies have demonstrated that stone comminution in SWL is a dynamic fatigue process (13) driven primarily by the local or average positive peak pressure [$p_{+(avg)}$] incident on the stone and facilitated by cavitation damage on the stone surface (12, 14, 15), thus favoring the acoustic field and cavitation characteristics of the HM3. Strong cavitation in renal or perirenal tissues, however, may increase the risk of adverse effects during SWL (16–18).

Significance

Electromagnetic (EM) shock wave lithotripters are widely used for noninvasive treatment of kidney stone patients. Here, we report the design of a new acoustic lens to rectify three fundamental drawbacks in contemporary EM lithotripters, based on in situ pulse superposition, leading to significantly improved stone comminution both in vitro and in vivo with minimal tissue injury. The new lens design improves the pressure distribution around the lithotripter focus with better alignment of the peak pressure and cavitation activities with the kidney stones under clinically relevant treatment conditions. The general principle of the new lens design is applicable to different lenses or reflectors and with further optimizations may enhance the performance and safety of contemporary EM lithotripters.

Author contributions: A.N., N.B.S., G.M.P., and P.Z. designed research; A.N., N.B.S., G.S., N.J.K., J.F.M., D.E.F., S.M., M.E.L., and W.N.S. performed research; A.N., N.B.S., D.E.F., S.M., W.N.S., and P.Z. contributed new reagents/analytic tools; A.N., N.B.S., G.S., D.E.F., S.M., M.E.L., G.M.P., and P.Z. analyzed data; and A.N., N.B.S., and P.Z. wrote the paper.

Conflict of interest statement: G.S., W.N.S., G.M.P., and P.Z. hold a patent entitled "Acoustic Lens for Shockwave Lithotripsy and Related Methods" on this technology, which is owned by Duke University.

This article is a PNAS Direct Submission.

[1]A.N. and N.B.S. contributed equally to this work.

[2]To whom correspondence should be addressed. E-mail: pzhong@duke.edu.

This article contains supporting information online at www.pnas.org/lookup/suppl/doi:10.1073/pnas.1319203111/-/DCSupplemental.

Another major drawback in contemporary lithotripters that has not been addressed is the significant shift in the locations of p_+ (i.e., acoustic focus) and peak negative pressure (p_-); the latter is associated with strong cavitation activity away from the geometric (or lithotripter) focus where kidney stones are positioned during SWL. In the HM3 (and other EH lithotripters), p_+ tends to shift postfocally up to 10 mm at high output settings, whereas p_- will shift prefocally by about 20 mm (11, 19–22). These opposite shifts in p_+ and p_- of EH lithotripters make it difficult to align the target stone concomitantly with the locations of p_+ and maximum cavitation activity, a scenario that will likely benefit stone comminution while reducing the risk of tissue injury (12, 23). In contrast, p_+ and p_- in EM lithotripters both shift prefocally with increased output energy, therefore providing an opportunity for better alignment with the target stone for improved treatment efficacy and safety.

In this study, we improve the lens design of a contemporary EM shock wave lithotripter to align its acoustic focus and region of maximum cavitation activity more closely to the target stone at clinically relevant high output settings. Additional features in lens modification that have been demonstrated in our pilot studies (10, 24) are simultaneously pursued to broaden the focal width and suppress the second compressive wave in the LSW profile, thereby overcoming the aforementioned fundamental drawbacks of EM lithotripters. Herein, we present in vitro and in vivo assessments of the efficacy and safety of the new lens design for a contemporary EM lithotripter.

Results

Lens Design. A polystyrene lens is used to focus a plane acoustic wave generated by an EM source. The original lens is in biconcave shape with an ellipsoidal (Fig. 1*A*) and a spherical (Fig. 1*B*) surface situated, respectively, distal and proximal to the EM source. For the new lens, an annular groove of depth h was cut in the spherical surface of the lens (Fig. 1*C*), leading to the elimination of the second compressive wave in the LSW profile via in situ pulse superposition and simultaneous broadening of the FW (10, 24). Optimal suppression of the second compressive wave and FW enlargement can be achieved by adjusting h and the area ratio (AR), defined in Eq. **S2**, between the uncut and total lens areas. After several prototypes, h = 14 mm and AR = 65% were selected as suitable geometric parameters for the new lens. To produce comparable and clinically relevant acoustic pulse energies in an area surrounding the target stone, the new lens must operate at a higher source voltage (i.e., 16–19 kV) than the one used for the original lens (i.e., 13–16 kV) to compensate for the acoustic energy loss caused by destructive in situ pulse superposition. However, significant prefocal shift in p_+ will occur at high output voltages owing to nonlinear wave propagation (25, 26).

To counteract the acoustic focal shift, the geometric focus of the new lens was set, after several trials, at 40 mm upwards from the geometric focus of the original lens, that is, the lithotripter focus (Fig. 1*C*). This modification allows the acoustic focus of the new lens to move gradually from 40 mm postfocally to about 5 mm prefocally in the full output voltage range (i.e., 10–19 kV) of the EM source. At low and medium output settings (i.e., 10–16 kV), distal positioning of the acoustic focus relative to the target stone will not increase the risk of tissue injury because of the associated low intensity, broad FW, and low peak pressures of the LSW. In comparison, the acoustic focus of the original lens will move in the same output range from the lithotripter focus to more than 25 mm closer to the source (Fig. 2*C*). By aligning the acoustic focus closely with the stone at high output settings, comminution efficiency may improve while the risk of tissue injury may be reduced. Specific modifications of the lens geometry are as follows: the spherical radius (R_s) and ellipsoidal semiminor axis (b_e) were changed from R_s = 220 mm and b_e = 95.03 mm, respectively, for the original lens to R_s = 350 mm and

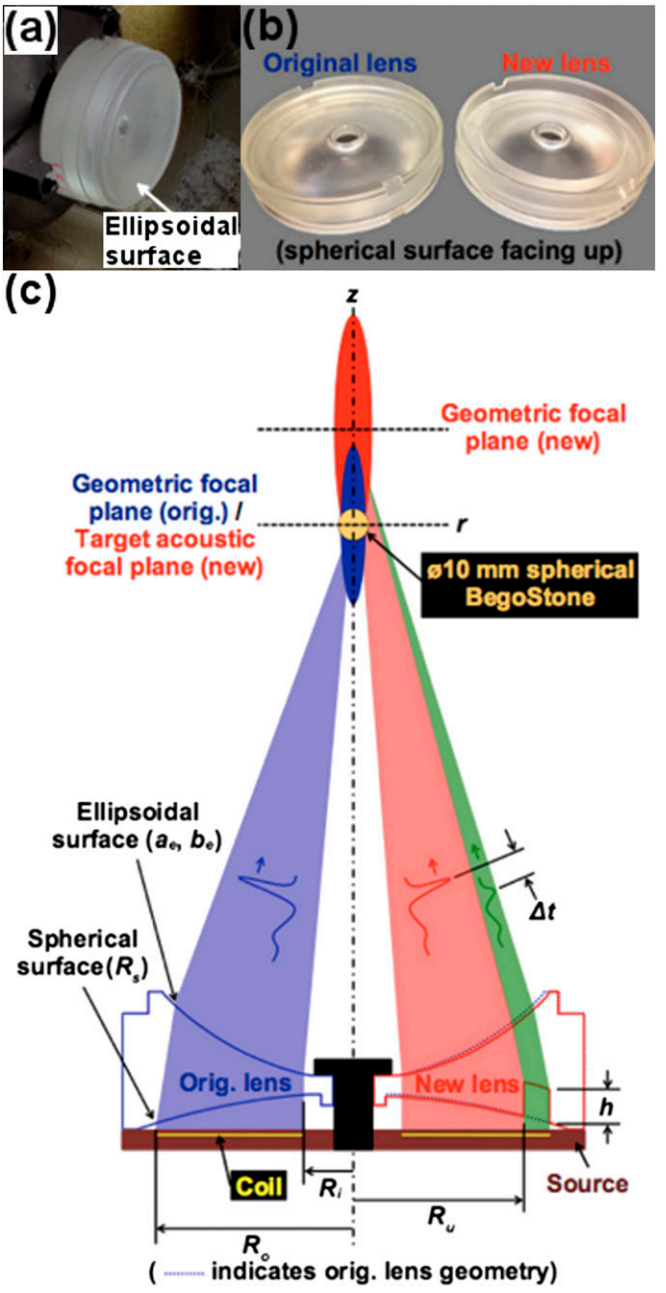

Fig. 1. Lens schematic. (*A*) Lens fabrication with ellipsoidal surface visible. (*B*) Finished lenses with spherical surfaces and annular ring cut of the new lens visible. (*C*) Sectioned illustration of both the original (*Left*) and new (*Right*) lenses with pertinent geometric parameters and corresponding acoustic effects indicated.

b_e = 102.03 mm for the new lens, whereas the ellipsoidal semimajor axis (a_e = 111.52 mm) remains unchanged. Details of the lens design modifications are shown in Fig. 1*C*.

In Vitro Characterization of Lenses. Characterizations of lithotripter focus and field parameters were carried out following standard protocols defined in IEC 61846 (27). For comparison of lens parameters, acoustic pulse energies were closely matched at the highest source voltage settings between the original lens (14.8 kV) and the new lens (18.1 kV) that did not produce severe adverse effects (i.e., subcapsular hematomas) in animal studies (see the discussion on in vivo experiments). Henceforth, all

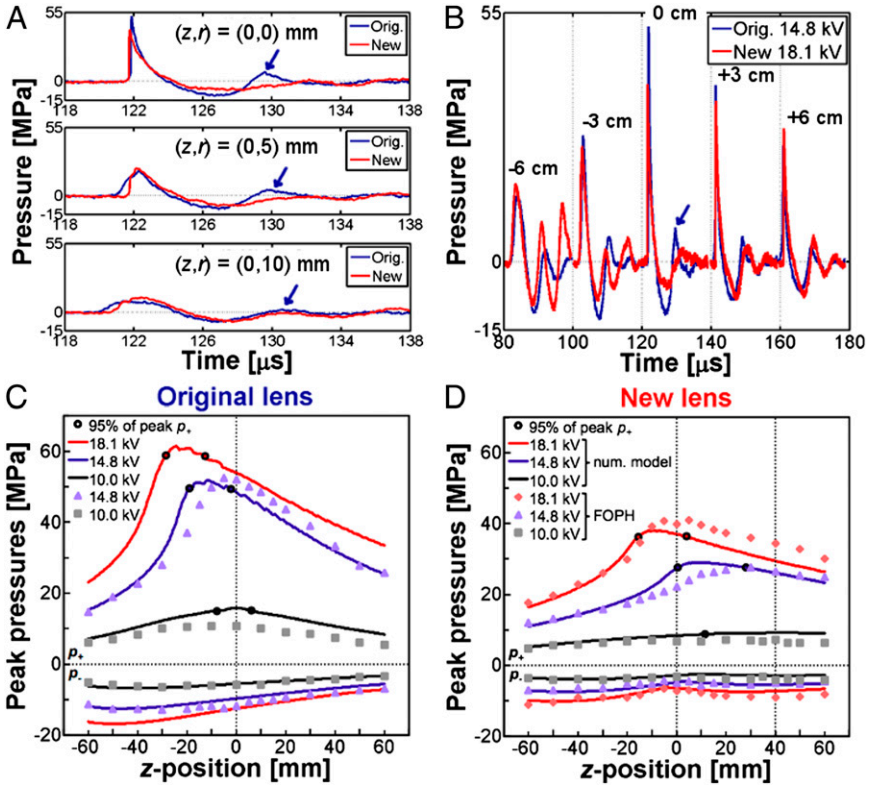

Fig. 2. Lens characterization. Averaged pressure waveforms at (*A*) three radial positions (r = 0, 5, and 10 mm) in the geometric focal plane of the original lens or lithotripter focal plane (z = 0 mm) and (*B*) positions along the central lithotripter (z) axis. Arrows indicate secondary compression in the original lens waveform at z = 0 mm; p_+ and p_- along the z axis at three different source voltages using the (*C*) original lens and (*D*) new lens. Continuous lines represent numerical model predictions of peak pressures and filled shapes indicate FOPH measurements; unfilled dark circles mark minimum uncertainty range for location of p_+ as predicted by numerical model. Vertical dotted lines indicate the geometric foci of the original (z = 0 mm) and new (z = +40 mm) lenses. For both lenses, z = 0 mm on the central axis coincides with the lithotripter focus where kidney stones are aligned during SWL.

comparisons between the new and original lenses were made under these high output settings unless otherwise specified. As shown in Table 1, the new lens has a 22% lower p_+ and 29% lower peak energy flux density with a 49% broader FW than the original lens. The new lens parameters (p_+ = 40 MPa, peak energy flux density = 0.6 mJ/mm^2, and FW = 11 mm) are similar to those reported for the HM3 (11, 28). Despite the significant differences in p_+, peak energy flux density and FW, the acoustic pulse energies produced by the two lenses are comparable in a circular area of radius R_c = 6 mm around the lithotripter focus (*SI Materials and Methods* and Fig. S1). Of interest, acoustic pulse energy associated with the leading compressive wave (E_+) is 8% higher for the new lens, which is within the measurement error (i.e., 10%) of the fiber optic probe hydrophone (FOPH) (29). Total acoustic pulse energy (E_{tot}), which encompasses energy contributions from the primary compression (E_+), tension (E_-), and secondary compression (E_{+2}), is 12% higher for the original lens. The most notable change in the energy content is that E_{+2} of the new lens is 85% less than that of the original lens, as a result of destructive in situ pulse superposition.

Representative pressure waveforms in the lithotripter focal plane (z = 0 mm) further demonstrate the significant cancellation of the second compressive wave by in situ pulse superposition (Fig. 2*A*). Pressure waveforms along the lithotripter axis (Fig. 2*B*) show the progressive evolution in the pulse profile of the two lenses. In particular, both constructive (z = −6 cm) and destructive (z = 0 cm) superposition of the leading LSW and the delayed wave generated by the cut region of the new lens is apparent. As a result of the lens modification, simultaneous lowering of p_+ and broadening of FW are evident from the peak pressure distribution in two orthogonal directions (Fig. S2 *A* and *B*). Proximal shift in p_+ can be seen with both the original (Fig. 2*C*) and new (Fig. 2*D*) lenses as the source voltage increases. The measured location of peak $|p_-|$ is ∼30 mm prefocal with the original lens and ≥60 mm with the new lens, although a minimum in $|p_-|$ occurs ∼5 mm prefocally, which corresponds to the location of strongest acoustic cancellation effects from in situ pulse superposition. The general trend in pressure distribution and acoustic focal shift has been confirmed by simulation results from a multiphysics model of shock wave focusing through the

Table 1. Comparison of representative technical parameters for the original and new lenses

Lens	Source voltage, kV	Lithotripter focus (z = 0 mm)		Global		FW, mm	Maximum energy flux density, mJ/mm^2	E_+, mJ	E_-, mJ	E_{+2}, mJ	E_{tot}, mJ
		p_+, MPa	p_-, MPa	p_+, MPa	z position, mm						
Original	14.8	52.0	−11.7	52.4	−5	7.4	0.84	39.5	19.9	2.0	61.6
New	18.1	39.8	−7.2	40.9	+5	11.0	0.59	42.5	11.7	0.3	55.0

original and new lenses (30). In the case of the original lens, the multiphysics model was used to estimate prefocal shift (~30 mm) at a high source voltage (18.1 kV) where FOPH measurements became impractical owing to interference from strong prefocal cavitation activity. At the highest source voltage measured (15.8 kV), peak p_+ was found to be located ~15 mm prefocally compared with ~5 mm prefocally at 14.8 kV. Although the acoustic focus will shift prefocally for both lenses in the dynamic range of the shock source (i.e., 10 ~19 kV), the specific modifications of the new lens ensure that at its highest output setting the acoustic focus will be closely matched (±5 mm) to the lithotripter focus where kidney stones are positioned during clinical SWL. Given a minimum of 5% uncertainty in pressure for both numerical model and FOPH results (29), the model predicted acoustic focal range of the new lens at 18.1 kV encompasses the lithotripter focus measured by FOPH (Fig. 2*D*). In contrast, the significant shift in acoustic focus of the original lens limits the highest voltage (i.e., <16 kV) that can be used safely for treatment of kidney stones.

Cavitation Assessment. Cavitation produced in the lithotripter field was captured by high-speed imaging, from which the bubble distribution probability, measured by cavitation index (CI) (*Materials and Methods*), and cavitation potential (31), measured by maximum bubble diameter, were quantified. Contour plots of CI for the original (Fig. 3*A*) and new (Fig. 3*B*) lenses were generated using the image frame corresponding to maximum bubble expansion (i.e., 250 μs). The maximum bubble lifetime near the lithotripter focus (indicated by "+" in Fig. 3) varies in the range of 400 ~ 450 μs, shown by representative high-speed images of bubble dynamics in a free field (Fig. 3). For the original lens, the fully developed bubble cloud covers a range from -71 mm $< z < -16$ mm, with a maximum cavitation index $CI_{o1} = 7.6\%$ observed at $z = -52$ mm. In comparison, the bubble cloud produced by the new lens spans a significantly greater area (both longitudinally and radially) with two distinct peaks: $CI_{n1} = 6.9\%$ at $z = -48$ mm and $CI_{n2} = 7.2\%$ at $z = +5$ mm. Similar to the original lens, the prefocal cavitation peak is produced primarily by the LSW from the uncut section of the new lens that superposes constructively with the delayed pulse in this region. The second peak in cavitation from the new lens is primarily the result of destructive superposition of LSW and delayed pulse, which eliminates the second compressive wave and thus boosts cavitation near the lithotripter focus. In fact, the maximum CI of the new lens at the lithotripter focus (CI = 7.0%) is significantly enhanced from that of the original lens (CI = 2.5%). In the perirenal region (z = −30 mm), bubble density is similar although marginally higher for the new lens (CI = 6.0%) compared with the original lens (CI = 5.6%). In the region typically aligned with patient skin ($z = -60$ mm) bubble density is comparable between the new lens (CI = 6.7%) and the original lens (CI = 6.6%). In terms of cavitation potential, the maximum bubble diameters measured throughout the lithotripter field are comparable. The representative values for the new and original lenses in different regions are 2.9 and 3.1 mm (-5 mm $< z < 5$ mm), 4.1 and 3.7 mm (-20 mm $< z < -40$ mm), and 4.3 and 4.4 mm (-50 mm $< z < -70$ mm), respectively. Overall, cavitation potentials produced by the two lenses are comparable, yet bubble density produced by the new lens in the lithotripter focal region is higher and covers a broader area, which may benefit stone comminution (12).

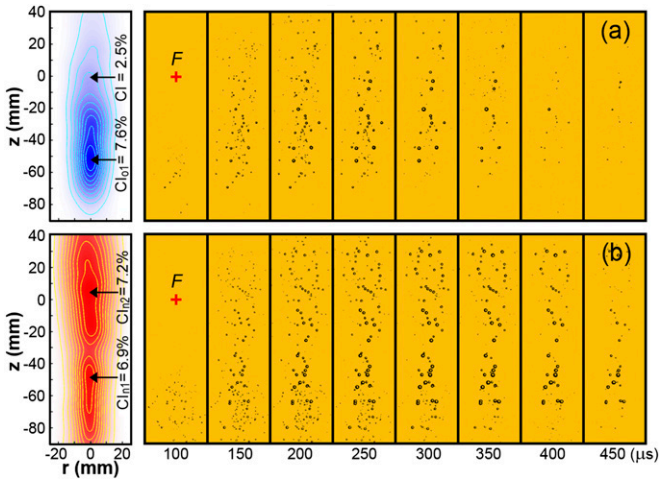

Fig. 3. Cavitation. Contour plots (*Left*) of CI obtained from an average of cavitation events produced by 30 consecutive lithotripter pulses produced by the (*A*) original lens and (*B*) new lens alongside representative bubble dynamics (*Right*) from a single cavitation event. Contours are generated from the frame corresponding to maximum bubble expansion (i.e., 250 μs). Lithotripter focus (F) is marked by "+." The width of each image frame is 50 mm.

In Vitro Stone Comminution. ***Under static conditions.*** Stone comminution was evaluated in vitro under static conditions where a 10-mm spherical BegoStone phantom was treated inside a flat-base tube holder (inner diameter 14 mm) at different positions in the lithotripter focal plane (Fig. 4*A*). At the focus ($r = 0$ mm), comminution efficiencies (<2.0 mm) after 1,000 shocks were 93 ± 4% for the new lens and 93 ± 3% for the original lens ($P = 1.00$). Comminution at $r = 5$ mm off-axis was also comparable, with 74 ± 10% for the new lens and 79 ± 9% for the original lens ($P = 0.58$). However, at $r = 10$ mm off-axis, stone comminution was statistically higher with 38 ± 9% for the new lens compared with 27 ± 8% for the original lens, with $P = 0.02$ (Fig. 4*B*). Average peak pressure incident on the stone during SWL was calculated as described previously (14), and the results showed that the new lens produces $p_{+(avg)}$ that is >30% higher than the original lens at $r = 10$ mm. Moreover, comminution efficiency at the beam focus was evaluated using a membrane holder with an inner diameter of 30 mm (Fig. S3*A*) to account for the effect of fragment spreading during SWL (11). Under such conditions, comminution efficiency (<2.0 mm) was 73 ± 10% for the new lens compared with 67 ± 8% for the original lens, with $P = 0.12$. However, when comminution efficiency was evaluated based on the percent of fragments <2.8 mm, the new lens (83 ± 9%) was found to be significantly better than the original lens (74 ± 9%), with $P = 0.05$ (Fig. S3*B*). Although the large diameter of the membrane holder increases substantially the uncertainty in fragment location and thus the exposure conditions during the treatment, the overall results suggest that the new lens produces finer fragments compared with the original lens. It is likely the large focal width with correspondingly high off-axial $p_{+(avg)}$ as well as strong cavitation activity generated by the new lens are all beneficial to comminution under conditions where stones/fragments may spread or drift significantly away from the beam focus.

Under the influence of simulated respiratory motion. The effect of respiratory motion on stone comminution was evaluated in vitro by translating the tube holder following various breath patterns (Fig. 4*C*). Using a dose of 1,000 shocks and two clinically relevant excursion distances of $D = 5$ and 15 mm (32), stone comminution (<2.0 mm) was compared between the original and new lenses (Fig. 4*D*). For a shallow breathing pattern ($D = 5$ mm), stone comminution efficiencies were statistically similar between the new (88 ± 5%) and original (86 ± 4%) lenses, with $P = 0.50$. At a normal respiratory excursion distance ($D = 15$ mm), the new lens produced statistically higher comminution efficiency of 82 ± 4% compared with 71 ± 6% for the original lens ($P < 0.01$). These results are in accordance with the observations from the static stone comminution experiments, indicating again that the

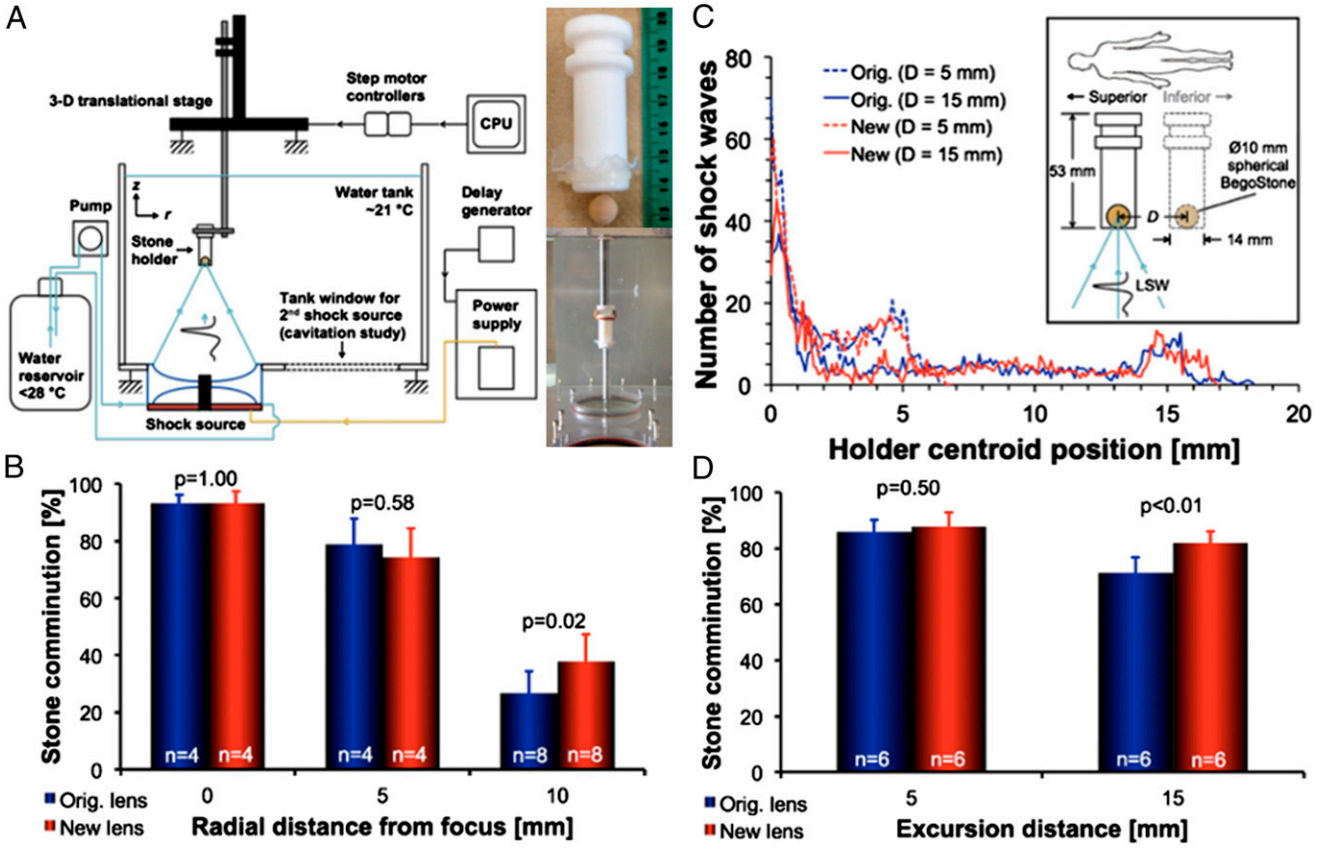

Fig. 4. In vitro stone comminution. (*A*) Schematic of the in vitro stone comminution experimental setup with tube holder depicted and pictured at right. (*B*) stone comminution results in the tube holder positioned at three radial distances in the lithotripter focal plane (r = 0, 5, and 10 mm). (*C*) Illustration of simulated respiratory motion (*Inset*) and average motion histograms corresponding to (*D*) stone comminution results at two excursion distances (D = 5 and 15 mm).

new lens has a much larger effective fragmentation area than the original lens within the lithotripter focal plane. Altogether, the new lens performs favorably under treatment conditions similar to those in vivo during SWL (i.e., stone translation owing to respiratory motion and fragments spreading inside the collecting system).

In Vivo Stone Comminution. Comminution efficiencies produced by the new and original lenses were further evaluated in vivo using a swine model. Cylindrical BegoStone phantoms [5 × 10 mm, diameter × length (D × L)] were surgically implanted in both kidneys before SWL (Fig. 5 *A* and *B*). A clinical ramping protocol was used (*SI Materials and Methods*) to deliver a total of 3,000 shocks at a pulse repetition frequency (PRF) of 1.5 Hz, corresponding to a total accumulated acoustic energy (calculated based on E_+) of ~112 J for each kidney. Overall, the new lens (12 renal units) produced a comminution efficiency of 72.8 ± 21.4% compared with 63.6 ± 21.8% for the original lens (10 renal units), with $P = 0.06$. However, when samples incidentally constrained by a double-J stent loop during the entire treatment (i.e., stones were prevented from spreading naturally) or those with abnormally large fragment displacement (i.e., migration to an off-focus calyx) were excluded, comminution efficiency became 88.8 ± 10.9% for the new lens (5 renal units) vs. 54.1 ± 23.3% for the original lens (6 renal units), with $P = 0.01$ (Fig. 5*C*).

Tissue Injury Assessment. Tissue injury was evaluated for the new lens in a pig model following the same clinical treatment protocol used in the stone comminution experiments with a few modifications: No stones were implanted in kidneys, SWL was performed at 1.0 Hz PRF, and only one kidney per pig was treated to avoid the influence of vasoconstriction on SWL-induced tissue injury (33). Overall, only minor skin lesions were observed at the LSW entrance region. A representative photograph of a swine flank shows a ~5-mm-wide region of altered skin with surrounding petechial bleedings (Fig. 6*A*), which is not atypical from SWL. Following SWL and in situ pressure fixation, the kidneys were harvested (Fig. 6*B*). Examinations of the anterior (Fig. 6*C*) and posterior (Fig. 6*D*) surfaces of the kidneys did not show any gross hematoma, nor was gross injury observed in other tissues (retro peritoneum, pancreas, spleen, and liver) near the kidney along the LSW blast path. These would all be a grade 0 based on a previously described grading scale for SWL injuries (34). From histology of the cortical area within the lithotripter beam focus (Fig. 6*E*), some subcapsular cell layers seemed to be detached as a result of a subtle degree of discohesion induced by mechanical stresses but did not show any sign of microscopic hemorrhage. Some characteristic microbleeding could be observed in the paramedullary cortex (Fig. 6*G*) and in a very small number of medullary tubules (Fig. 6*H*), consistent with typical injury from SWL in the deep cortex (35, 36). With no evidence of severe tissue injury from either microscopic or gross examinations, the new lens is considered safe for SWL at the aforementioned output settings.

Discussion

The goal of this study is to improve the performance of a contemporary EM lithotripter through modifications of lens geometry that can be easily implemented without altering the lithotripter

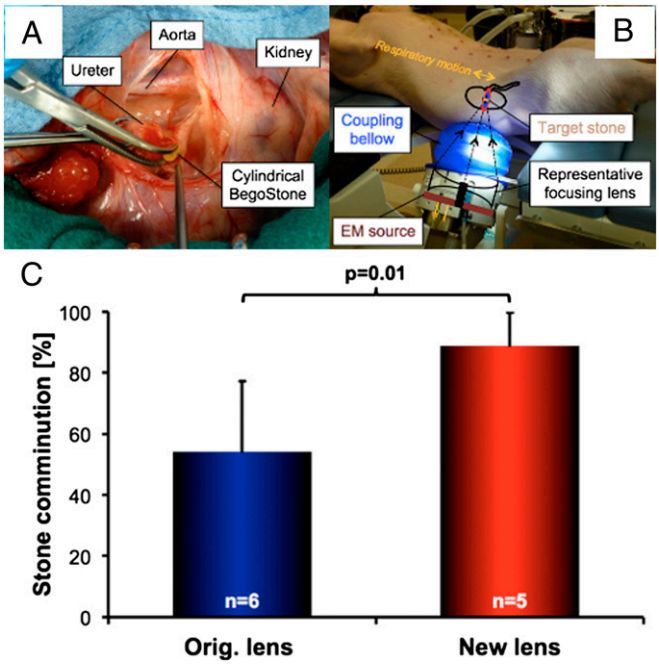

Fig. 5. In vivo stone comminution. (*A*) Implantation of a cylindrical BegoStone phantom (5 × 10 mm, D × L) into the renal pelvis via an incision in the ureter of a pig model. (*B*) Typical setup for SWL therapy with the animal in supine position and shock source coupling bellow inflated to establish contact with the pig; a drawing of the main lithotripter components, acoustic focusing angle, and target kidney is overlaid. (*C*) In vivo stone comminution results from subgroups after eliminating outliers.

focus and other system components, making this upgrade simple and cost-effective for clinical translation. The new lens design addresses several fundamental drawbacks in contemporary EM lithotripters, namely, the misalignment of p_+ and region of peak cavitation activity with the lithotripter focus at high output settings, narrow FW, and nonidealized LSW profile. In comparison with the original lens, both in vitro and in vivo results have demonstrated the advantage of the new lens with improved stone comminution and minimal tissue injury at a clinically relevant high output setting. The general principle in lens modification and associated implementation strategy described in this work are also applicable to design improvement of other EM lithotripters equipped with either convex lenses (37) or parabolic reflectors (38).

The design and technical refinements of EM lithotripters from the late 1980s to middle 1990s were largely driven by empirical experience, practical concern for user convenience, and multifunctionality of the lithotripter system (39, 40). The transition of SWL technology during this period from EH to predominately EM was carried out by lithotripter manufacturers with an incomplete understanding about the mechanisms of tissue injury and stone comminution in SWL (41). Consequently, clinical experience with the third-generation EM lithotripters, characterized by high p_+ and small FW, often resulted in low stone comminution efficiency with high retreatment rate compared with the original HM3 (9, 38, 41, 42). Attempts to boost stone comminution by significantly augmenting the output pressure or energy of the lithotripter have been unsuccessful, which is likely associated with the greater risk of hematoma formation in the perirenal region at high output settings (35). Because shear stress (43, 44) and cavitation (16–18, 23) are two primary mechanisms of tissue injury, the significant prefocal shift in p_+ and strong cavitation activity in the perirenal region of contemporary EM lithotripters will likely limit the range of output pressure or energy that can be safely applied to renal stone treatment in clinical SWL.

The new lens design addresses misalignment of p_+ and peak cavitation activity with the lithotripter focus at high output settings through in situ pulse superposition and reshaped lens geometry, confirmed by FOPH measurements (Fig. 2*D*) and high-speed imaging (Fig. 3*B*). In addition, the improved alignment of p_+ with the target stone using the new lens may help reduce tissue injury in the perirenal region from strong shock-induced shearing (43), supported by in vivo results under clinically relevant output conditions (Fig. 6). A second region of maximum cavitation produced by the new lens is located ∼5 cm anterior to the lithotripter focus, similar to that produced by the original lens (Fig. 3). In patients, this region is typically covered by skin and muscles, which are less susceptible to cavitation damage than perirenal tissues. Furthermore, bubbles produced in the coupling bellow of the lithotripter may be removed by a jetting flow with further modification in lithotripter design (45).

Despite a significant increase in CI at lithotripter focus (i.e., $z = 0$ cm), the maximum CI of the new lens does not exceed the corresponding value for the original lens (i.e., $CI_{n2} \leq CI_{o1}$ in Fig. 3), suggesting that the new lens is comparatively safe. This observation is further supported by similar measurements of maximum bubble radii produced by the two lenses. Effective acoustic cancellation from superposition of the primary LSW and delayed wave of the new lens occurs around $z = 0$ cm. A local minimum in peak negative pressure ($|p_-|$) near to the focal region (evident in Fig. 2 *B* and *D*) is indicative of strong destructive wave interference. Prefocally ($z < 0$ cm), the difference in arrival times (Δt) between the LSW and delayed wave to the central axis is sensitive to differences in the travel distance between acoustic rays emanating from the inner and outer lens sections, which result in a larger Δt than at $z = 0$ cm and apparent constructive interference of waveforms near z = −6 cm (Fig. 2*B*). In effect, cavitation activity from the new lens is similar to that of the original lens in this region, because secondary compression of the primary LSW and primary compression of the delayed wave superpose to offset relatively high $|p_-|$. Postfocally ($z > 0$ cm), the discrepancy in Δt becomes increasingly negligible, and the new lens pulse profile approaches the original lens pulse profile. The merging of LSW and delayed wave in this region may be the result of nonlinear wave interaction. Overall, varying wave interactions in the field produce banded concentrations of cavitation bubbles, similar to other observations from dual-pulse lithotripsy (46, 47).

In contemporary EM lithotripters, a second compressive wave in the LSW profile counteracts the preceding tensile wave and suppresses bubble growth (10, 24). The new lens design has corrected this general drawback, leading to a more idealized LSW pulse profile similar to that of the HM3 and stronger cavitation activity in the lithotripter focal plane (Fig. 2*A* and Fig. 3). Moreover, cavitation activity is substantially wider both longitudinally and radially using the new lens, the latter of which may be beneficial to the erosion of fragments within the focal plane that spread after the initial fracture. The broadening of cavitation activity with the new lens is mirrored by a ∼49% enhancement of its focal width compared with the original lens. These features may work together to improve stone comminution efficiency with the new lens, through synergistic interactions between LSW-induced stress waves and cavitation pitting produced on the stone surface (12, 14, 48, 49).

Previous studies have shown that lithotripters with narrow FW and high peak pressure are less effective in stone comminution if significant respiratory motion (50) or spreading of residual fragments (11) occurs during SWL. In contrast, lithotripters with broad FW and low peak pressure are effective and safe for SWL (51–53). These observations have been corroborated by recent findings that stone comminution in SWL is driven by the average

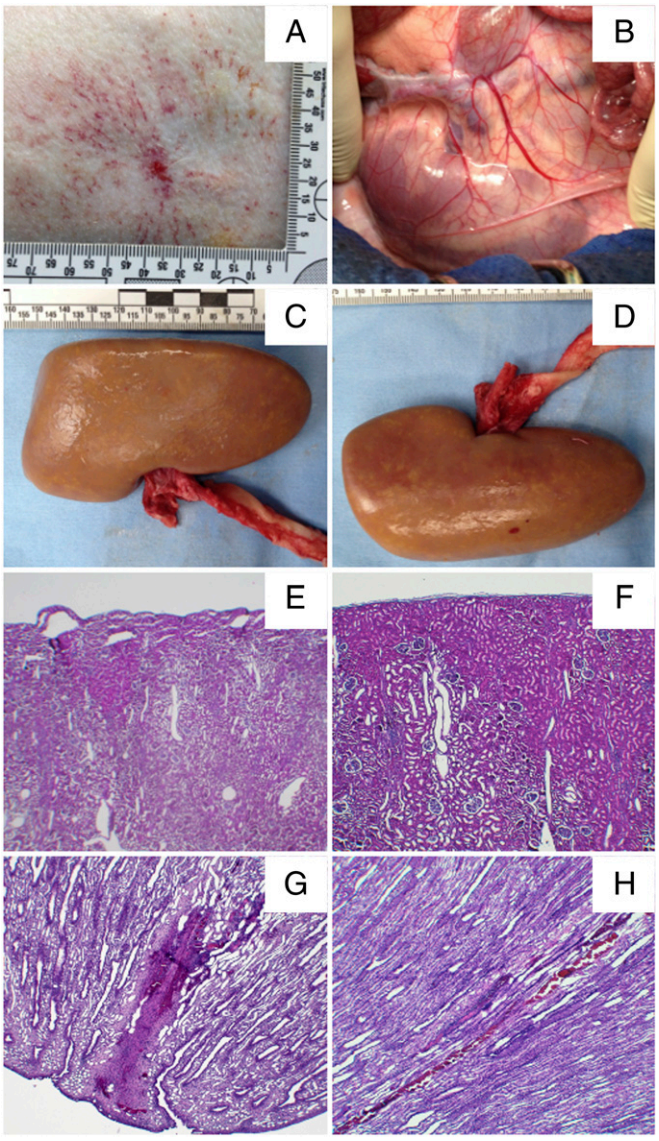

Fig. 6. Tissue Injury produced by the new lens. (*A*) Representative skin lesion at the shock head coupling area. (*B*) Retroperitoneum after SWL treatment. Macroscopic pictures of the (*C*) anterior and (*D*) posterior kidney surfaces with capsule removed (posterolateral red dot is a ruptured nutritive vessel from capsule removal). Lateral cortex histology images (*E*) within the path of the LSW and (*F*) far off-axis. (*G*) Characteristic bleeding in the medullary pyramid and (*H*) a small number of medullary tubules.

(or local) peak pressure incident on the stone (as opposed to the global peak pressure in the lithotripter field) that exceeds a minimal pressure threshold to initiate fracture (14). Therefore, for the maximally allowable acoustic energy that can be safely delivered to the kidney, a lithotripter with a broad FW and lower peak pressure will have a larger fragmentation zone in the focal plane than its counterpart with narrow FW and high peak pressure (11, 54). Results of our in vitro stone comminution experiments at $r = 10$ mm off-axis and in the membrane holder support this notion (Fig. 4*B* and Fig. S3*B*). Clinically, it is well known that kidney stones can move up to 5 cm during inspiration and expiration breath phases (8), which can result in 30–40% of shock waves missing the target stone (55, 56). The benefits of a lithotripter field with broad FW, associated high average peak pressure, and strong cavitation activity are supported by the results of in vitro respiratory motion simulations where for excursions of 15 mm the new lens produced statistically higher stone comminution than the original lens (Fig. 4*D*). Furthermore, stone comminution results in vivo have demonstrated that the new lens is more effective than the original lens in an environment that simultaneously allows for stone movement from respiration and spreading (Fig. 5*C*). The extent of swine respiration under general anesthesia, estimated from fluoroscopic imaging, resembles more closely a shallow excursion (e.g., D = 5 mm) than normal human respiration (e.g., D = 15 mm), which suggests the possibility of further improvements in human trials using the new lens.

Altogether, the new acoustic lens design described in this work has addressed several fundamental drawbacks characteristic of contemporary EM shock wave lithotripters. By eliminating the second compressive wave through in situ pulse superposition, a stronger, wider, and more uniformly distributed cavitation field is produced near the target stone. By reshaping the lens surfaces, the location of p_+ and peak cavitation activity at high source voltages is corrected from the prefocal perirenal and subcapsular region of the kidney to the lithotripter focus. Finally, by reducing the aperture of the primary LSW, the focal zone is broadened, resulting in significantly improved in vitro and in vivo stone comminution efficiency and minimal tissue injury at a clinically relevant high output setting. Further optimization of the new lens design may be carried out to decrease cavitation potential at the skin surface to ensure effective transmission of the LSW from the source into the patient. Alternatively, the new lens can be used at low to medium energy settings to reduce discomfort to the patient. With these encouraging preliminary results, future patient studies are warranted to determine the performance and safety of the new lens design in clinical trials.

Materials and Methods

Lens Design and Fabrication. The geometry of the original lens of a Siemens EM shock wave lithotripter (Modularis; Siemens) was modified to produce the new lens. First, an annular groove of depth h = 14 mm and AR = 65% was cut into the spherical surface (i.e., the side that is proximal to the source) of the lens near its periphery (*SI Materials and Methods* and Fig. 1*C*). This modification is adapted from a pilot study on in situ pulse superposition using an EM shock wave lithotripter for simultaneous FW enhancement and pulse profile alteration (10). The second and third geometric modifications to the acoustic lens pertain to acoustic focal shift along the central lithotripter axis. Both the spherical radius (R_s = 350 mm) and ellipsoidal semiminor axis (b_e = 102.03 mm) were enhanced from the original lens configuration (R_s = 220 mm and b_e = 95.03 mm) to produce a longer geometric focal length in the new lens design. The semimajor axis (a_e = 111.52 mm) was consistent between the two lenses. To estimate the acoustic focusing distance of the new lens at various source voltages, a multiphysics computational model of wave propagation for EM shock wave lithotripters was used (see *SI Materials and Methods* for further details and Fig. 2 *C* and *D* for representative computational results) (30). After determination of critical geometric parameters from pilot experiments and modeling, the new lens was machined from a 6–inch-diameter solid cylinder of Rexolite 1422 cross-linked polystyrene (*SI Materials and Methods*). The new lens was subsequently inserted into a standard Modularis housing unit for in vitro and in vivo testing.

In Vitro Characterization of Lenses. Details of the in vitro lithotripter characterization procedures using a FOPH (FOPH 500; RP Acoustics) have been described previously (14). Hydrophone data postprocessing to determine relevant lithotripter parameters such as −6 dB FW (i.e., full width at half maximum peak pressure) and E_+ followed the IEC 61846 protocol for lithotripter field characterization (27), described in short in *SI Materials and Methods*. Manufacturer-specified uncertainty in calibrated and postprocessed FOPH measurements is ∼5% in pressure and ∼10% in energy.

Cavitation Assessment. In vitro cavitation produced in the lithotripter field was captured by shadowgraph imaging using a Phantom 7.3 high-speed camera (Vision Research) at a framing rate of 20,000 frames per second with 10-μs exposure time. Bubble dynamics were recorded in a region of interest (ROI) centered around the lithotripter axis that spans from the skin entrance to postkidney (-110 mm $< z <$ 40 mm) with a radius about 25 mm. To ensure

comparable water quality during the experiments, two identical shock sources equipped with either the original or new lens were mounted side by side at the bottom of the Lucite tank and used alternately so that all of the measurements could be done within 30 min. Cavitation produced by either source in free field was recorded during 30 consecutive lithotripter pulses using a slow PRF of 0.05 Hz to provide sufficient interpulse time for residual bubble remnants to dissolve in water before the arrival of the next LSW (46, 57). Using this strategy, combined with carefully regulated water temperature and dissolved gas concentration in the tank, the interaction between individual bubbles was minimized. The image sequences were analyzed offline using a custom program written in MATLAB. The results from 30 experimental runs were superimposed, from which the average projected area of cavitation bubbles in the ROI during the maximum bubble expansion, referred to here as CI, was calculated following methods described previously (58, 59).

Stone Comminution. The following applies to all in vitro and in vivo stone comminution experiments. The original lens was operated at a source voltage of 14.8 kV, compared with 18.1 kV with the new lens. The large dynamic range of the Modularis lithotripter (up to 19.3 kV) accommodates the increase in source voltage, which is necessary to equilibrate acoustic pulse energies delivered to the lithotripter focus within a radius of 6 mm by the two lenses. Comparable acoustic energies ($E_+ \approx 40$ mJ) were used for each lens during stone comminution experiments (Table 1) because it has been shown that stone comminution efficiency correlates closely with the pulse or accumulated acoustic energy in SWL (51, 60, 61). BegoStone phantoms used during comminution experiments were fabricated with a 5:1 powder-to-water mixing ratio following a previously described protocol to mimic the physical properties of hard kidney stones such as calcium oxalate monohydrate and brushite stones (62). After SWL treatment, fragments were collected, carefully rinsed, air-dried for at least 24 h, sieved sequentially with standardized mesh sizes of 4, 2.8, and 2 mm, and weighed. Comminution efficiency was determined by the percent in weight of fragments less 2 mm (unless otherwise specified) normalized by the pretreatment weight of the stone. The results are presented as mean ± SD. For statistical analysis, a two-tailed Student *t* test was used.

In Vitro Stone Comminution. A 3D positioning system (VXM-2 step motors with BiSlide-M02 lead screws;Velmex) was used for precise alignment of two stone holders used for in vitro comminution tests, facilitated by a mechanical pointer that coincides with the lithotripter focus (Fig. 4*A*). In all of the experiments, precise stone alignment was performed and 1,000 shocks were delivered at a PRF of 1.0 Hz. To assess stone comminution at different lithotripter field positions, 10-mm spherical BegoStone samples were treated in a flat-base tube holder (inner diameter 14 mm) in the lithotripter focal plane either on the *z* axis ($r = 0$ mm) or at two off-axis positions ($r = 5$ and 10 mm). At least four samples were treated at each position, and for off-axis positions multiple treatments were carried out in four quadrants to minimize potential bias in holder misalignment (14). To account for the effect of fragment spreading, additional experiments were repeated at the lithotripter focus using a pressure-release membrane holder with an inner diameter of 30 mm (*SI Materials and Methods* and Fig. S3 *A* and *B*). The in vitro setup was further used to assess the effect of respiratory motion on stone comminution following a protocol described in *SI Materials and Methods* (54, 63).

In Vivo Stone Comminution. The Institutional Animal Care and Use Committee of Duke University approved all in vivo study protocols for stone comminution and tissue injury assessment. The procedure for stone comminution using cylindrical BegoStone phantoms (D × L = 5 × 10 mm) has been described previously and can be found in detail in *SI Materials and Methods* (24). For comparison of in vivo comminution rates between the two lenses, a two-tailed Student *t* test was used after excluding outliers with an interquartile range of 1. A subgroup analysis was performed considering experimental biases as described in *Results* and *SI Materials and Methods*.

Tissue Injury Assessment. For tissue injury assessment, six female farm pigs (~50 kg) were used to demonstrate the safety of the new lens at a clinically relevant, high-output setting (i.e., 18.1 kV). Only a single (left) kidney was treated in each pig to avoid the uncertain influence of SWL-induced vasoconstriction on the degree and severity of tissue injury in the contralateral kidney (33). Three thousand shock waves were applied at a PRF of 1.0 Hz using an otherwise identical SWL treatment protocol used for in vivo stone comminution experiments. The pigs were killed within 2 h of completion of SWL. The kidneys were cannulated and perfused in situ with saline followed by 10% neutral buffered formalin, then removed *en bloc*. The harvested and perfusion-fixed kidneys were immersed in 10% neutral buffered formalin and further fixed for at least 7 d before postprocessing as described in *SI Materials and Methods* (24).

In histological analysis, the pathologist examined the original slides microscopically and correlated the location of all findings with the virtual whole mount images. Microscopic examination included the entire SWL target site for each kidney, all adjacent areas showing evidence of injury, and representative areas of unaffected tissue. Particular attention was directed to the presence of tissue necrosis, hemorrhage, evidence of cell injury (including ballooning, vacuolation, and cell dropout), and mechanical tissue injury (including tearing of blood vessels or liquefaction of adipose tissue; Fig. 6).

ACKNOWLEDGMENTS. The authors thank Joseph Kleinhenz, Jaclyn Lautz, and Tim Schykowski for their technical support and Siemens for providing the electromagnetic shock wave generators and original lenses. This work was supported by National Institutes of Health Grant R37-DK052985-17 (to P.Z.) and Ferdinand Eisenberger Grant NeA1/FE-11 from the Deutsche Gesellschaft für Urologie (to A.N.).

1. Chaussy C, Brendel W, Schmiedt E (1980) Extracorporeally induced destruction of kidney stones by shock waves. *Lancet* 2(8207):1265–1268.
2. Scales CD, Jr., Smith AC, Hanley JM, Saigal CS; Urologic Diseases in America Project (2012) Prevalence of kidney stones in the United States. *Eur Urol* 62(1):160–165.
3. Stamatelou KK, Francis ME, Jones CA, Nyberg LM, Curhan GC (2003) Time trends in reported prevalence of kidney stones in the United States: 1976–1994. *Kidney Int* 63(5):1817–1823.
4. Taylor EN, Stampfer MJ, Curhan GC (2005) Diabetes mellitus and the risk of nephrolithiasis. *Kidney Int* 68(3):1230–1235.
5. Taylor EN, Stampfer MJ, Curhan GC (2005) Obesity, weight gain, and the risk of kidney stones. *JAMA* 293(4):455–462.
6. Rassweiler JJ, et al. (2011) Shock wave technology and application: An update. *Eur Urol* 59(5):784–796.
7. Wilbert DM, et al. (1987) New generation shock wave lithotripsy. *J Urol* 138(3): 563–565.
8. Lingeman JE, McAteer JA, Gnessin E, Evan AP (2009) Shock wave lithotripsy: Advances in technology and technique. *Nat Rev Urol* 6(12):660–670.
9. Gerber R, Studer UE, Danuser H (2005) Is newer always better? A comparative study of 3 lithotriptor generations. *J Urol* 173(6):2013–2016.
10. Zhong P, Smith N, Simmons NW, Sankin G (2011) A new acoustic lens design for electromagnetic shock wave lithotripters. *10th International Symposium on Therapeutic Ultrasound* (*Istu 2010*), (American Institute of Physics, Melville, NY), Vol 1359, pp 42–47.
11. Qin J, Simmons WN, Sankin G, Zhong P (2010) Effect of lithotripter focal width on stone comminution in shock wave lithotripsy. *J Acoust Soc Am* 127(4):2635–2645.
12. Zhu S, Cocks FH, Preminger GM, Zhong P (2002) The role of stress waves and cavitation in stone comminution in shock wave lithotripsy. *Ultrasound Med Biol* 28(5): 661–671.
13. Lokhandwalla M, Sturtevant B (2000) Fracture mechanics model of stone comminution in ESWL and implications for tissue damage. *Phys Med Biol* 45(7):1923–1940.
14. Smith N, Zhong P (2012) Stone comminution correlates with the average peak pressure incident on a stone during shock wave lithotripsy. *J Biomech* 45(15):2520–2525.
15. Zhong P (2013) Shock wave lithotripsy. *Bubble Dynamics and Shock Waves*, ed Delale CF (Springer, Berlin), pp 291–338.
16. Dalecki D, et al. (1997) The influence of contrast agents on hemorrhage produced by lithotripter fields. *Ultrasound Med Biol* 23(9):1435–1439.
17. Delius M, et al. (1990) Biological effects of shock waves: Cavitation by shock waves in piglet liver. *Ultrasound Med Biol* 16(5):467–472.
18. Matlaga BR, et al. (2008) Potential for cavitation-mediated tissue damage in shockwave lithotripsy. *J Endourol* 22(1):121–126.
19. Sokolov DL, et al. (2002) Prefocal alignment improves stone comminution in shockwave lithotripsy. *J Endourol* 16(10):709–715.
20. Averkiou MA, Cleveland RO (1999) Modeling of an electrohydraulic lithotripter with the KZK equation. *J Acoust Soc Am* 106(1):102–112.
21. Coleman AJ, Saunders JE (1993) A review of the physical properties and biological effects of the high amplitude acoustic field used in extracorporeal lithotripsy. *Ultrasonics* 31(2):75–89.
22. Zhou Y, Zhong P (2006) The effect of reflector geometry on the acoustic field and bubble dynamics produced by an electrohydraulic shock wave lithotripter. *J Acoust Soc Am* 119(6):3625–3636.
23. Zhong P, Zhou Y, Zhu S (2001) Dynamics of bubble oscillation in constrained media and mechanisms of vessel rupture in SWL. *Ultrasound Med Biol* 27(1):119–134.
24. Mancini JG, et al. (2013) Assessment of a modified acoustic lens for electromagnetic shock wave lithotripters in a swine model. *J Urol* 190(3):1096–1101.
25. Karzova MM, Averiyanov MV, Sapozhnikov OA, Khokhlova VA (2012) Mechanisms for saturation of nonlinear pulsed and periodic signals in focused acoustic beams. *Acoust Phys* 58(1):81–89.

26. Makov YN, et al. (2006) Strong on-axis focal shift and its nonlinear variation in low-Fresnel-number ultrasound beams. *J Acoust Soc Am* 119(6):3618–3624.
27. International Electrotechnical Commission (1998) Ultrasonics – pressure pulse lithotripters – characteristics of fields. *International Standard 61846* (International Electrotechnical Commission, Geneva).
28. Coleman AJ, Saunders JE (1989) A survey of the acoustic output of commercial extracorporeal shock wave lithotripters. *Ultrasound Med Biol* 15(3):213–227.
29. Smith N, et al. (2012) A comparison of light spot hydrophone and fiber optic probe hydrophone for lithotripter field characterization. *Rev Sci Instrum* 83(1):014301.
30. Fovargue DE, et al. (2013) Experimentally validated multiphysics computational model of focusing and shock wave formation in an electromagnetic lithotripter. *J Acoust Soc Am* 134(2):1598–1609.
31. Iloreta JI, Zhou Y, Sankin GN, Zhong P, Szeri AJ (2007) Assessment of shock wave lithotripters via cavitation potential. *Phys Fluids (1994)* 19(8):86103.
32. Bromage PR, Bonsu AK, el-Faqih SR, Husain I (1989) Influence of Dornier HM3 system on respiration during extracorporeal shock-wave lithotripsy. *Anesth Analg* 68(3): 363–367.
33. Handa RK, et al. (2009) Pretreatment with low-energy shock waves induces renal vasoconstriction during standard shock wave lithotripsy (SWL): A treatment protocol known to reduce SWL-induced renal injury. *BJU Int* 103(9):1270–1274.
34. Rassweiler J, et al. (1993) Experimental basis of shockwave-induced renal trauma in the model of the canine kidney. *World J Urol* 11(1):43–53.
35. Connors BA, et al. (2012) Evaluation of shock wave lithotripsy injury in the pig using a narrow focal zone lithotriptor. *BJU Int* 110(9):1376–1385.
36. Handa RK, et al. (2009) Assessment of renal injury with a clinical dual head lithotriptor delivering 240 shock waves per minute. *J Urol* 181(2):884–889.
37. Bohris C, Jensen H, Bayer T, Liong ML (2006) A new integrated ultrasound system for shockwave lithotripsy. *J Endourol* 20(11):863–869.
38. Zehnder P, et al. (2011) A prospective randomised trial comparing the modified HM3 with the MODULITH® SLX-F2 lithotripter. *Eur Urol* 59(4):637–644.
39. Lingeman JE (1997) Extracorporeal shock wave lithotripsy. Development, instrumentation, and current status. *Urol Clin North Am* 24(1):185–211.
40. Rassweiler J, et al. (1992) Lithotripter technology - Present and future. *J Endourol* 6(1): 1–13.
41. Lingeman JE, Kim SC, Kuo RL, McAteer JA, Evan AP (2003) Shockwave lithotripsy: Anecdotes and insights. *J Endourol* 17(9):687–693.
42. Graber SF, Danuser H, Hochreiter WW, Studer UE (2003) A prospective randomized trial comparing 2 lithotriptors for stone disintegration and induced renal trauma. *J Urol* 169(1):54–57.
43. Freund JB, Colonius T, Evan AP (2007) A cumulative shear mechanism for tissue damage initiation in shock-wave lithotripsy. *Ultrasound Med Biol* 33(9):1495–1503.
44. Howard D, Sturtevant B (1997) In vitro study of the mechanical effects of shock-wave lithotripsy. *Ultrasound Med Biol* 23(7):1107–1122.
45. Lautz J, Sankin G, Zhong P (2013) Turbulent water coupling in shock wave lithotripsy. *Phys Med Biol* 58(3):735–748.
46. Arora M, Junge L, Ohl CD (2005) Cavitation cluster dynamics in shock-wave lithotripsy: part 1. Free field. *Ultrasound Med Biol* 31(6):827–839.
47. Sokolov DL, Bailey MR, Crum LA (2001) Use of a dual-pulse lithotripter to generate a localized and intensified cavitation field. *J Acoust Soc Am* 110(3 Pt 1):1685–1695.
48. Sapozhnikov OA, Maxwell AD, MacConaghy B, Bailey MR (2007) A mechanistic analysis of stone fracture in lithotripsy. *J Acoust Soc Am* 121(2):1190–1202.
49. Sass W, et al. (1991) The mechanisms of stone disintegration by shock waves. *Ultrasound Med Biol* 17(3):239–243.
50. Cleveland RO, Anglade R, Babayan RK (2004) Effect of stone motion on in vitro comminution efficiency of Storz Modulith SLX. *J Endourol* 18(7):629–633.
51. Eisenmenger W (2001) The mechanisms of stone fragmentation in ESWL. *Ultrasound Med Biol* 27(5):683–693.
52. Eisenmenger W, et al. (2002) The first clinical results of "wide-focus and low-pressure" ESWL. *Ultrasound Med Biol* 28(6):769–774.
53. Pishchalnikov YA, et al. (2013) Evaluation of the LithoGold LG-380 lithotripter: In vitro acoustic characterization and assessment of renal injury in the pig model. *J Endourol* 27(5):631–639.
54. Smith NB, Zhong P (2013) A heuristic model of stone comminution in shock wave lithotripsy. *J Acoust Soc Am* 134(2):1548–1558.
55. Leighton TG, et al. (2008) A passive acoustic device for real-time monitoring of the efficacy of shockwave lithotripsy treatment. *Ultrasound Med Biol* 34(10):1651–1665.
56. Sorensen MD, et al. (2012) Quantitative assessment of shockwave lithotripsy accuracy and the effect of respiratory motion. *J Endourol* 26(8):1070–1074.
57. Sapozhnikov OA, et al. (2002) Effect of overpressure and pulse repetition frequency on cavitation in shock wave lithotripsy. *J Acoust Soc Am* 112(3 Pt 1):1183–1195.
58. Cleveland RO, Sapozhnikov OA, Bailey MR, Crum LA (2000) A dual passive cavitation detector for localized detection of lithotripsy-induced cavitation in vitro. *J Acoust Soc Am* 107(3):1745–1758.
59. Sankin GN (2006) Cavitation under spherical focusing of acoustic pulses. *Acoust Phys* 52(1):93–103.
60. Delius M, Ueberle F, Gambihler S (1994) Destruction of gallstones and model stones by extracorporeal shock waves. *Ultrasound Med Biol* 20(3):251–258.
61. Granz B, Köhler G (1992) What makes a shock wave efficient in lithotripsy? *J Stone Dis* 4(2):123–128.
62. Esch E, et al. (2010) A simple method for fabricating artificial kidney stones of different physical properties. *Urol Res* 38(4):315–319.
63. Davies SC, Hill AL, Holmes RB, Halliwell M, Jackson PC (1994) Ultrasound quantitation of respiratory organ motion in the upper abdomen. *Br J Radiol* 67(803):1096–1102.

Supporting Information

Neisius et al. 10.1073/pnas.1319203111

SI Materials and Methods

Lens Design and Fabrication. The annular ring modification of the lens design delays the propagation of the outer portion of an incident plane wave generated by the EM coil by a time step

$$\Delta t = h \cdot \left(\frac{1}{c_0} - \frac{1}{c_l}\right), \qquad \text{[S1]}$$

where c_l (2.40 km/s) and c_0 (1.49 km/s) are the longitudinal (or P) wave speeds in the lens and water, respectively. The inner portion of the incident plane wave is refracted through the central, uncut region of the lens, forming the new leading lithotripter shock wave (LSW). Because of the reduced source aperture, the focal width (FW) of the leading LSW is broadened while superposition of the time-delayed wave with the leading LSW alters the pulse profile (1). The inner radius of the annulus (R_u = 56.2 mm) determines the area ratio of uncut to total lens surface, that is,

$$AR = \frac{R_u^2 - R_i^2}{R_o^2 - R_i^2}, \qquad \text{[S2]}$$

where R_i (16.9 mm) and R_o (68.6 mm) are radii of the lens aligned to the inner and outer edges of the coil within the source, respectively (Fig. 1*C*).

The acoustic focusing distances produced by spherical and ellipsoidal lens surface modifications were estimated using a multiphysics computational model of wave propagation. The model employs a finite-volume conservation law Riemann solver (2) within the BEARCLAW framework developed by S.M. and solves the linear elasticity and Euler equations simultaneously to simulate wave propagation within the focusing lens and water domains, respectively. Input plane wave pressure for the numerical model was measured using a fiber optic probe hydrophone (FOPH) and curve-fitted as described previously (3). As a derivation of FOPH measurements, uncertainty in numerical model results is 5% at minimum (4).

The 3D shape of the acoustic lens was designed using Autodesk Inventor CAD software and then exported to MasterCam (CNC Software), where the material removal machining motions were programmed. Using a Centroid CNC lathe and carbide turning tools, the excess material was removed in 2-mm steps to form the shape of the new lens. After machining, all surfaces of the lens were polished using an ultrafine aluminum silicate polishing pad (Scotch Brite 9767; 3M).

In Vitro Characterization of Lenses. Acoustic fields produced by the original and new lenses were characterized using the FOPH, which was fastened to a 3D positioning stage controlled remotely using a program written in MATLAB (MathWorks). The axisymmetric electromagnetic (EM) shock source with either the original or new lens was mounted at the base of a Lucite tank (length × width × height, 43 × 39 × 29 cm) filled with 0.2-μm-filtered and degassed water (<3 mg/L O_2 concentration, ~21 °C). Pressure waveforms were measured in four quadrants in the lithotripter focal plane using radial step sizes of 1 mm ($0 < r < 6$ mm) and 2 mm ($6 < r < 14$ mm). Along the lithotripter (z) axis, pressure waveforms were measured in 5-mm intervals (-20 mm $< z < +20$ mm) and 10-mm intervals (-60 mm $< z < -20$ mm and $+20$ mm $< z < +60$ mm). FOPH waveforms were recorded at 100-MHz sampling frequency using a LeCroy Waverunner 6050a digital oscilloscope (Teledyne LeCroy) and transferred for off-line calibration and postprocessing using MATLAB. *FW* was calculated as the full width at half maximum peak pressure (p_+), and the derived total acoustic pulse energy was determined by

$$E_{tot} = \frac{2\pi}{Z_0} \cdot \int_0^{R_c} \int_{t_1}^{t_2} p_a(r,t)^2 \cdot r dt dr, \qquad \text{[S3]}$$

where Z_0 (1.5 MRayls) is the acoustic impedance of water, R_c (6 mm) is a radius encompassing most stones treated with shock wave lithotripsy (SWL), $p_a(r,\tau)$ is acoustic pressure from the LSW, and time values (t_1 and t_2) are the first and final crossing points of 10% of the local p_+ by the $p_a(r,t)$. Eq. **S3** is also used to calculate compressive and secondary acoustic pulse energies, with t_1 and t_2 defined as the first and final crossing points of 10% of the local p_+ by the applicable wave section.

In Vitro Stone Comminution. In membrane holder experiments, a 20-gauge syringe needle sandwiched between the edge of two membranes (Fig. S2*A*) was used to allow for pressure release inside the membrane holder, which reduces fluid and fragment mixing effects during SWL (5). In simulated respiratory motion experiments, the 3D positioning system was used to translate the flat-base tube holder along a single horizontal axis within the lithotripter focal plane during SWL. Four different phases of respiration (i.e., inspiration, inspiration pause, expiration, and expiration pause) were simulated following typical kidney motion patterns observed in patients (6). The holder was translated in the inferior direction (away from the lithotripter focus) during inspiration and returned in the superior direction to the focal region during expiration (Fig. 4*C*). The simulated breath rate (12 breaths per minute) and excursion distances (D = 5 or 15 mm) were representative of kidney displacement in patients during SWL under heavy or light sedation, respectively (7). Randomization factors were incorporated to avoid discrete translation patterns. Histograms of the motion patterns used during comminution tests were statistically similar between the two lenses (Fig. 4*C*).

In Vivo Stone Comminution. Female farm pigs with an approximate weight of 50 kg were used as animal models because their kidney size and anatomy are similar to those of human kidneys (8). Eleven pigs were used to compare fragmentation efficiency produced by the Siemens Modularis EM lithotripter using either the original or new lens. Animals were placed under general endotracheal anesthesia and shaved along their flanks to improve coupling quality across the skin surface. Subsequently, animals were transferred to an operation table for midline laparotomy. After bowel mobilization, the retroperitoneal space was opened to expose the proximal ureter close to the renal pelvis. A proximal ureterotomy of ~1 cm was performed, and a cylindrical BegoStone phantom was inserted and guided into the renal pelvis (Fig. 5*A*). Through the existing ureterotomy, a 6-french polyurethane double-J ureteral stent (Boston Scientific) was advanced into the renal pelvis to prevent stone and fragment migration to the ureter during and after SWL. The ureterotomy was closed with a 4/0 running monofilament suture. This procedure was repeated on the opposite kidney. After closing the laparotomy, the animal was transferred to the lithotripsy table.

Before SWL, ultrasound gel (Medline) was applied on the coupling bellow of the shock head, and the lithotripter focus was

aligned to an implanted stone under fluoroscopic guidance (Fig. 5*B*). The bellow was then carefully inflated to establish skin contact to minimize air pockets trapped at the coupling interface. Afterward, a constant bellow pressure was maintained (9) during the entire therapy session in which 3,000 shocks were delivered to each kidney at a pulse repetition frequency of 1.5 Hz. In the first 800 shocks, a ramping scheme of incrementally increasing acoustic pulse energy was used, which has been successfully used in clinics for patient treatment (10, 11). After the initial 500 shocks, the treatment was paused for 4 min before resuming at higher output levels, which has been suggested as a protective measure against SWL-induced tissue injury in animal models (12). From 800 to 3,000 shocks, the maximum source voltage (i.e., 14.8 kV for the original lens or 18.1 kV for the new lens) was applied, resulting in ~112 J of cumulative acoustic pulse energy (E_+) delivered to the focal region. Stone movement and spreading were checked with fluoroscopy in situ after 200, 500, 800, and 1,000 shocks. To avoid potential operator bias to the comminution results, no realignment of lithotripter focus was performed after 500 shocks, even when fragments spread to different (upper or lower) calyces after the initial fracture. Post-SWL, the pigs were killed. Ureters were ligated to avoid any loss of fragments, and the kidneys were harvested and bivalved. Each sample was photographed, and fragments were collected for analysis. In comparisons of in vivo comminution rates, a subgroup analysis was performed to consider experimental biases from either incidental confinement of stones by double-J stent loop during the entire treatment (i.e., stones that were prevented from spreading naturally) or abnormal fragment spread (i.e., large fragment migration to an off-focus calyx).

Tissue Injury Assessment. Following general anesthesia of the animal, a cystoscopy was performed to place an open-ended 6-french ureteral catheter (Cook Medical) in a retrograde fashion into the kidney collecting system. To align the lithotripter focus to the lower part of the middle calyx of each kidney, fluoroscopic agent Isoview-300 (Bracco Diagnostics) was injected through the catheter. After complete drainage of the contrast medium, SWL was performed. Post-SWL, the skin surface at the LSW entrance site was photographed. Following killing and kidney excision, additional photographs were taken from the anterior and posterior sides of the kidneys, as well as surrounding organs/tissues to document any visible gross injury.

For microscopic tissue injury assessment, fully fixed kidneys were serially sliced in the coronal plane at 3-mm intervals. Both surfaces of each slice were photographed. Slices that included the SWL target site as well as other areas showing evidence of injury were divided into 2- × 2-cm blocks for histologic processing using a numbered grid to facilitate reassembly of stained section images into a virtual organ of whole mount slices. These blocks were processed and paraffin-embedded, and 5-μm-thick sections were stained with hematoxylin and eosin. All resulting sections were imaged at high resolution (2,400 pixels per inch) using a digital flat-bed scanner (PIXMA MP470; Canon), and the resulting images were assembled into virtual whole mount images using Photoshop CS3 (Adobe Systems) supplemented by Fovea Pro-4.0 (Reindeer Graphics).

1. Zhong P, Smith N, Simmons NW, Sankin G (2011) A new acoustic lens design for electromagnetic shock wave lithotripters. *10th International Symposium on Therapeutic Ultrasound* (*Istu 2010*), (American Institute of Physics, Melville, NY), Vol 1359, pp 42–47.
2. LeVeque RJ (1997) Wave propagation algorithms for multidimensional hyperbolic systems. *J Comput Phys* 131(2):327–353.
3. Smith N, et al. (2012) A comparison of light spot hydrophone and fiber optic probe hydrophone for lithotripter field characterization. *Rev Sci Instrum* 83(1):014301.
4. Fovargue DE, et al. (2013) Experimentally validated multiphysics computational model of focusing and shock wave formation in an electromagnetic lithotripter. *J Acoust Soc Am* 134(2):1598–1609.
5. Qin J, Simmons WN, Sankin G, Zhong P (2010) Effect of lithotripter focal width on stone comminution in shock wave lithotripsy. *J Acoust Soc Am* 127(4):2635–2645.
6. Davies SC, Hill AL, Holmes RB, Halliwell M, Jackson PC (1994) Ultrasound quantitation of respiratory organ motion in the upper abdomen. *Br J Radiol* 67(803):1096–1102.
7. Bromage PR, Bonsu AK, el-Faqih SR, Husain I (1989) Influence of Dornier HM3 system on respiration during extracorporeal shock-wave lithotripsy. *Anesth Analg* 68(3): 363–367.
8. Connors BA, et al. (2012) Evaluation of shock wave lithotripsy injury in the pig using a narrow focal zone lithotriptor. *BJU Int* 110(9):1376–1385.
9. Neucks JS, et al. (2008) Improved acoustic coupling for shock wave lithotripsy. *Urol Res* 36(1):61–66.
10. Zhou YF, Cocks FH, Preminger GM, Zhong P (2004) The effect of treatment strategy on stone comminution efficiency in shock wave lithotripsy. *J Urol* 172(1):349–354.
11. Maloney ME, et al. (2006) Progressive increase of lithotripter output produces better in-vivo stone comminution. *J Endourol* 20(9):603–606.
12. Connors BA, et al. (2009) Effect of initial shock wave voltage on shock wave lithotripsy-induced lesion size during step-wise voltage ramping. *BJU Int* 103(1): 104–107.

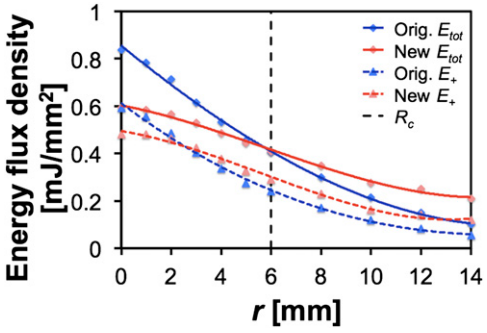

Fig. S1. Energy flux density. A comparison of energy flux densities curve-fitted with trinomials, which are used in the calculation of total acoustic pulse energy (E_{tot}) and compressive acoustic pulse energy (E_+) for the original and new lenses. R_c is the radius for pulse energy calculation and represents a threshold that encompasses most stones treated with SWL.

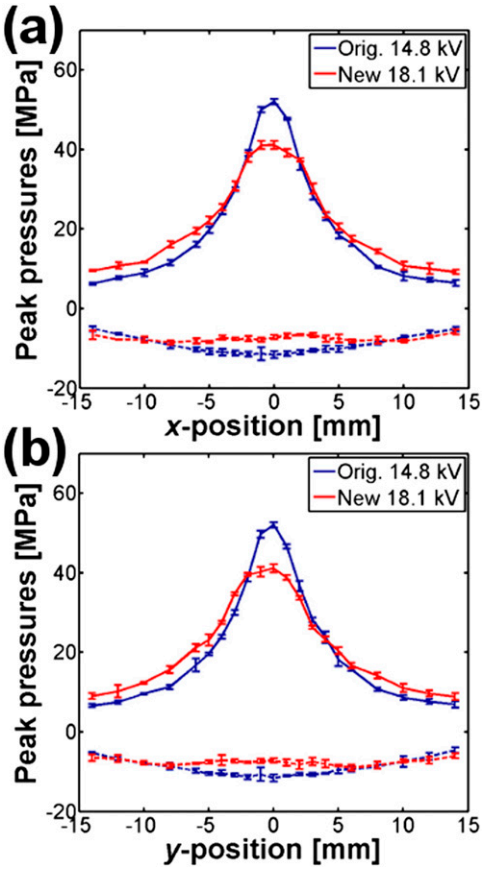

Fig. S2. Lens characterization. Averaged peak positive (p_+) and negative (p_-) pressures at $z = 0$ mm measured along the (*A*) *x* and (*B*) *y* axes of the symmetric EM source.

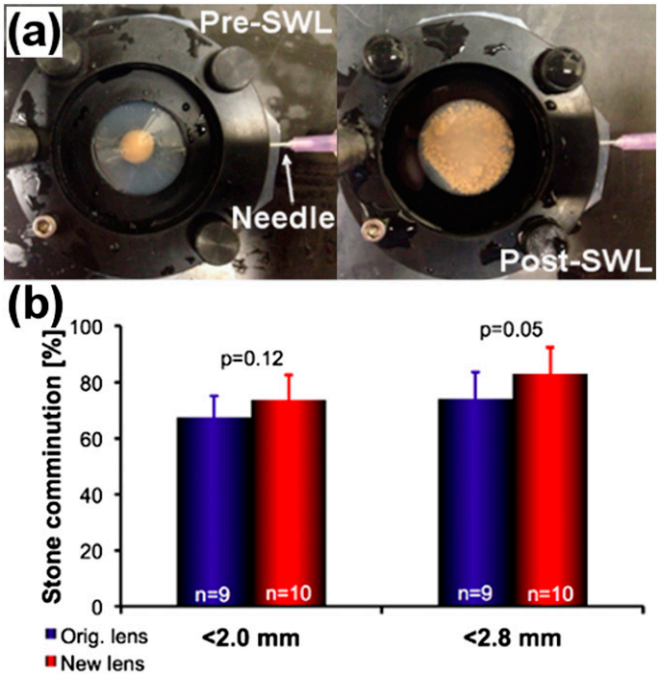

Fig. S3. In vitro stone comminution. (*A*) Representative (*Left*) pre- and (*Right*) post-SWL images of stone comminution in the membrane holder positioned at the lithotripter focus. (*B*) Stone comminution results in the membrane holder using two mesh sizes for fragment collection.